



Publication Year	2016
Acceptance in OA	2020-05-20T15:50:19Z
Title	Exploring high-z galaxies with the E-ELT
Authors	GULLIEUSZIK, MARCO, Falomo, R., GREGGIO, Laura, USLENGHI, MICHELA, FANTINEL, Daniela
Publisher's version (DOI)	10.1051/0004-6361/201628114
Handle	http://hdl.handle.net/20.500.12386/25015
Journal	ASTRONOMY & ASTROPHYSICS
Volume	593

Exploring high- z galaxies with the E-ELT

M. Gullieuszik¹, R. Falomo¹, L. Greggio¹, M. Uslenghi², and D. Fantinel¹

¹ INAF, Osservatorio Astronomico di Padova, Vicolo dell'Osservatorio 5, 35122 Padova, Italy
e-mail: marco.gullieuszik@oapd.inaf.it

² INAF, Istituto di Astrofisica Spaziale e Fisica Cosmica, via Bassini 15, 20133 Milano, Italy

Received 12 January 2016 / Accepted 14 June 2016

ABSTRACT

We present simulated observations of galaxies at $z = 2$ and $z = 3$ to probe the capabilities of next-generation telescopes (E-ELT and JWST) to measure the structural and photometrical properties of high-redshift galaxies. We carry out an extensive set of simulations of high-redshift galaxies adopting the specifications of the E-ELT first light instrument MICADO. The main parameters (sizes, Sersic index, and magnitudes) of the galaxies are measured using GALFIT and the accuracy of the determinations is assessed by comparing the input values to the measurements from many runs with different statistical noise. We also address the effects on the accuracy of the measurements of possible spatial variation of the point spread function (PSF) in the field. We find that from $3h$ exposure E-ELT near-infrared (IR) images of galaxies at $z \sim 2$ and $z \sim 3$ it will be possible to measure the size, total magnitude, and galaxy morphology with an accuracy of 2–5% for objects as faint as $H \sim 25$ and half-light size of 0.2 arcsec. The effective radius of compact, early-type galaxies is also recovered with $\sim 5\%$ accuracy, provided that their half-light size exceeds 20 mas. These results are compared with those expected from simulated observations obtained with NIRCcam on board the JWST.

Key words. instrumentation: adaptive optics – techniques: photometric – galaxies: fundamental parameters – galaxies: high-redshift – galaxies: photometry

1. Introduction

Understanding the assembly history of galaxies is of paramount importance for answering fundamental questions about the processes of formation and evolution of galaxies and their associations (groups, clusters, superclusters, etc.). To this end, it is of extreme relevance to be able to characterise the properties of galaxies at high redshift to probe their evolution over a significant interval of cosmic time. Their global structure and colours yield insight into the conditions of star formation and the subsequent merger events and/or secular processes (e.g. Dalcanton et al. 1997; Mo et al. 1998).

Although galaxies usually comprise multiple different components (i.e. bulges, disks, substructures) fitting their surface brightness profile with a single Sersic law can provide relevant basic data (e.g. Kelvin et al. 2012). This is in particular needed for the study of distant galaxies that are poorly resolved with current ground-based telescopes and partially available with *Hubble* Space Telescope (HST; e.g. van der Wel et al. 2012).

Unfortunately the characterisation of photometrical and structural properties of high- z objects is hampered by the faintness of the targets and by their very small angular size. HST observations have shown that galaxies at high- z are significantly smaller in size than galaxies of similar mass at low z (e.g. Daddi et al. 2005; Trujillo et al. 2006; Buitrago et al. 2008; Vulcani et al. 2014; Kennedy et al. 2015) and this size evolution ($R_e \sim (1+z)^{-1}$) with redshift, furthermore, hinders the capability of studying the structural properties of these galaxies. In fact present estimates of galaxy size at $z \gtrsim 2$ yield apparent sizes of ~ 100 – 200 mas or less. At higher redshift the situation is even more challenging since the angular size of the galaxies become smaller than 50 mas (Ono et al. 2013). As a consequence, it is now possible to characterise these galaxies only via HST ob-

servations, but this is limited to galaxies with mass $\gtrsim 10^{10} M_\odot$ (Brammer et al. 2012; van der Wel et al. 2012, 2014, and refs therein). In spite of the diffraction limit images obtained by HST, the size of these high-redshift galaxies is so small that a significantly better spatial resolution is needed to be able to properly characterise their structure. A major improvement in this direction is expected by future observations gathered by the *James Webb* Space Telescope (JWST), which also has the important advantage of an extremely low background in the near-infrared (IR). Because of the relative small aperture (6.5 m), however, the JWST resolution is limited to few hundredths of arcsec. A more significant step is expected by the future generation of extremely large ground-based optical/near-IR telescopes. In fact these 30–40 m aperture telescopes assisted by adaptive optics can reach resolution of few mas in the near-IR.

In this paper we aim to address the imaging capabilities of the planned future instrumentation for Extremely Large Telescopes (ELTs) using the expected performances of the Multi-Adaptive Optics Imaging Camera for Deep Observations (MICADO; Davies et al. 2010) at the European Extremely Large Telescope (E-ELT)¹ as a reference. We quantify the accuracy with which it will be possible to characterise the properties of high-redshift galaxies with simulated MICADO observations. In particular these simulations are used to investigate the possibility to accurately measure both the size and morphology of the galaxies. Moreover using multi-band observations we estimate the accuracy that could be achieved in the measurements of the colour gradient; this is a key tool to test models of galaxies formation. In fact the colour gradients trace variations of the properties of stellar populations, and are linked to

¹ <http://www.eso.org/sci/facilities/eelt/>

the star formation history of galaxies (see e.g. Saglia et al. 2000; Tamura et al. 2000; Kobayashi 2004; Gargiulo et al. 2011).

Finally, the results obtained with simulated E-ELT observations are compared with those expected for the same targets from observations secured with the Near-Infrared camera (NIRcam) on board the JWST². Throughout this paper, we adopt a concordance cosmology with $H_0 = 70 \text{ km s}^{-1} \text{ Mpc}^{-1}$, $\Omega_m = 0.3$, and $\Omega_\Lambda = 0.7$. All magnitudes are in AB system.

2. Simulations of high- z galaxies

In order to assess the accuracy with which it will be possible to characterise the galaxy properties from observations with ELTs, we analyse simulated images of high-redshift galaxies assuming a wide range of photometric and structural parameters. The comparison between the observed photometric and structural parameters and the true (input) values yields insights on the statistical and systematic effects.

2.1. Input models

In this work we assume simple smooth models for the simulation of galaxies. In particular Sersic models with various different parameters are chosen to study the effects for a variety of cases. More complex models (e.g. substructures, knots, and tails) are not considered, as our main objective is to investigate the capability to derive the main global parameters (luminosity, scale-length, and morphology) of high-redshift galaxies.

The Sersic law is defined by the following expression:

$$\mu(r) = \mu_e + 2.5 \frac{b_n}{\ln(10)} [(r/R_e)^{1/n} - 1] \quad (1)$$

$$\mu_e = M_{\text{tot}} + 2.5 \log \left[(1 - e) 2\pi R_e^2 \right] + 2.5 \log \left[n e^{b_n} \Gamma(2n) / b_n^{2n} \right], \quad (2)$$

where M_{tot} is the total magnitude, e the ellipticity, Γ the complete gamma function, and the value of b_n is such that

$$2\gamma(2n, b_n) = \Gamma(2n), \quad (3)$$

where γ is the incomplete gamma function (for details see Ciotti 1991).

ELTs combined with adaptive optics systems will deliver the best performances in the near-IR. Therefore we performed two sets of simulations in the J , H , and K bands to map the $U - V$ rest-frame colour of galaxies at $z \sim 2.3$ (J and H bands) and at $z \sim 3.3$ (H and K bands). In the following, we refer to these two sets of simulations as $z = 2$ and $z = 3$, respectively. To test the dependence of the results on the galaxy size and morphology, we considered 27 template galaxies with nine values of the total mass in the range $9 < \log M/M_\odot < 11$ and three values of the Sersic index, $n = 1.0, 2.5$, and 4.0 .

The relationships among the structural parameters (R_e and μ_e) and the galaxy masses for galaxies of the different morphological types were calibrated following the results of van der Wel et al. (2014), who presented measurements for a sample of 30 000 galaxies from the CANDELS HST survey with redshift $0 < z < 3$. For simulations of $z = 2$ galaxies, we used the mean loci of $z = 2.25$ galaxies. For simulations of $n = 1.0$ and $n = 4.0$ galaxies, we used the scaling relations for late-type and early-type galaxies, respectively. For $n = 2.5$ galaxies, we adopted the intermediate (average) values of above relationships. The parameters for the simulated galaxies at $z = 3$ were defined

by extrapolating the scaling relations of van der Wel et al. (2014) at redshift $z = 3.3$. We used an ellipticity of 0.3 and a 90° position angle (major axis along the horizontal direction) for all galaxies. The complete list of adopted parameters for the simulated galaxies are shown in Fig. 1 and reported in Tables A.1 and A.2.

2.2. Image simulations

Simulated images of galaxies were produced using the Advanced Exposure Time Calculator (AETC)³ tool (Falomo et al. 2011). We adopt as baseline the parameters of MICADO, the instrument designed for the 39-m aperture E-ELT to provide quasi-diffraction limited imaging over a wide ($\sim 1'$) field of view. The simulations of MICADO observations were performed following the same prescription as in Gullieuszik et al. (2014). We used the point spread functions (PSFs) of the multi-conjugate adaptive optics post focal relay (MAORY; Diolaiti et al. 2010) for the E-ELT, calculated for a $0''.6$ seeing at the centre of the corrected field of view (FoV). These were produced for the final design of MAORY phase A study.

The final simulated images were obtained as the stack of 180 individual images of 60 s exposure for a total exposure time of three hours. To evaluate the effect of the statistical noise, we performed 50 runs for each simulated galaxy and then compared the resulting parameters for all the simulations.

Some examples of simulated galaxies of different mass and morphology and their azimuthally averaged radial surface brightness profiles are shown in Figs. 2 and 3. The images for all simulated galaxies are available in Figs. A.1–A.3.

3. Results

For each galaxy we measured the photometric (total magnitude) and structural parameters (effective radius R_e , Sersic index n , ellipticity, and position angle) using GALFIT (Peng et al. 2002). The first guess for each parameter was randomly chosen from a distribution of values centred on the input value and with a dispersion of 30%. We tested that even with first guess parameters that deviate largely from the input values, the fitted values do not change from those reported in this analysis.

A crucial ingredient for this analysis is the assumed PSF. In fact since the size of the distant galaxies is very small (a fraction of arcsec), the effects of the PSF on the shape of the galaxies is significant. In this work, for the GALFIT measurements, we assumed the simulated image of a bright star as PSF, which is obtained with AETC in the same configuration adopted for the galaxies. This is clearly an ideal situation and any additional source of instability (variable seeing, performance of the AO system, etc.) of the *real* observations will likely degrade the performances of the whole system. We start by evaluating the accuracy of the measurements in this ideal case; some effects due to variable PSF are discussed in Sect. 3.2.

From the GALFIT analysis of each simulated galaxy, we measured the R_e , n , and total magnitude, and compared these values with the true parameters. For each galaxy model we derive the mean and standard deviation of the difference of the parameters using the 50 independent runs. The results are given in Tables A.3 for the case at $z = 2$ and A.4, for $z = 3$.

² <http://www.stsci.edu/jwst/instruments/nircam>

³ <http://aetc.oapd.inaf.it/>

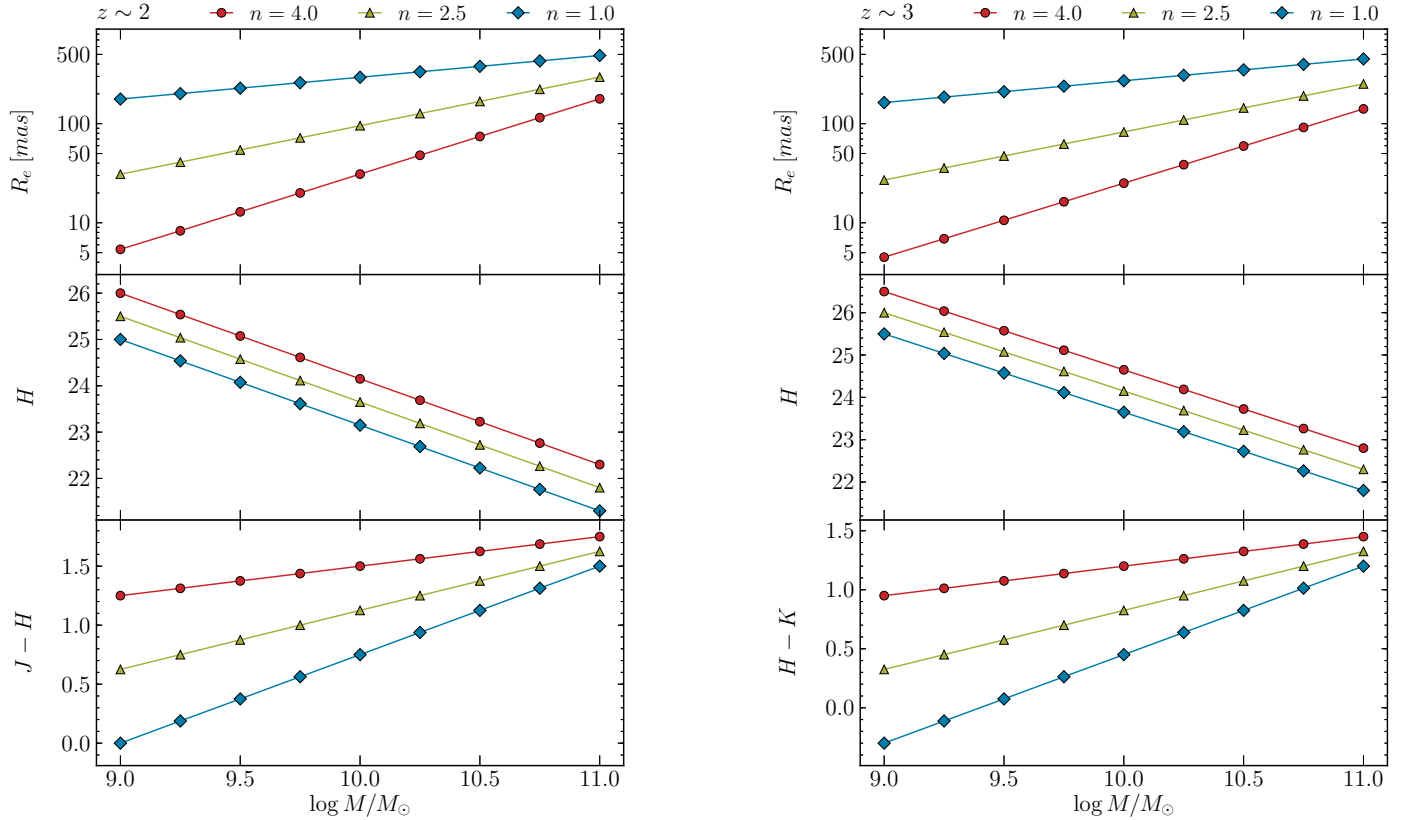


Fig. 1. Structural and photometric parameters adopted for the two sets of simulated galaxies at $z = 2$ (left panels) and $z = 3$ (right panels). For each set we plot the relation between the galaxy mass and effective radii in milli-arcseconds (top panel), magnitude (middle panel), and colour (bottom panel) for the 9 template galaxies. In each panel we show the scaling relations for galaxies with 3 different Sersic index with different colours and symbols (see the legend on top of the figure).

3.1. Galaxy structural parameters

In Figs. 4 and 5 we summarise the results of the capability of determining the structural parameters of high-redshift galaxies for different morphology (Sersic index) and mass or size. It turns out that, under the conditions described above, with the combination of sensitivity and spatial resolution of MICADO, it will be possible to characterise galaxies at $z = 2$ and $z = 3$ with an accuracy better than $\sim 10\%$ and for objects with masses as low as 10^9 to $10^{10} M_\odot$ (depending on morphology and redshift; see details in Figs. 4 and 5). The most critical objects are those at higher redshift that are also more compact (high Sersic indices). Actually, in both figures we only report the uncertainties of the galaxies with size large enough to be measured. The effective radius of early-type galaxies ($n = 4$) at $z = 2$ is measured with an accuracy of $\sim 3\%$ (5%) in the H (J) band, for masses higher than $6 \times 10^9 M_\odot$. A similar accuracy is found for early-type galaxies at redshift $z = 3$, provided that they are more massive than $10^{10} M_\odot$. Objects for which these uncertainties apply are greater in size than ~ 20 mas, and their magnitudes and Sersic indices are also very well determined.

For late-type galaxies ($n = 1$ and 2.5) at both redshifts, the effective radius can be recovered with an accuracy better than 5% over the whole explored mass range and actually better than 2% for the largest disks ($n = 1$). The Sersic index and total magnitude of late-type galaxies are also recovered with a good accuracy for all masses at both $z = 2$ and 3 with a tendency to worsen at low masses in the $z = 3$ case. At this high redshift, it appears that measurements in the K band will yield results that are less accurate (Fig. 5 right panel) owing to the relatively high

contribution of the IR background. Conversely, in the H band, low mass, star-forming galaxies with a shallow surface brightness profile ($n < 2.5$) have effective radii of ~ 100 mas and can be measured with an accuracy better than $\sim 5\%$, however, their large size also implies a fainter average surface brightness or a lower signal-to-noise ratio. Nevertheless since these galaxies very often appear clumpy their substructures will be relatively easy to detect (see example in Sect. 3.5). Since the galaxy population at high- z is expected to be dominated by disk/star-forming galaxies the assumed imaging capabilities of MICADO will be adequate to study in detail the bulk of galaxy population up to $z \sim 3$ and beyond. Besides the statistical errors, we note some systematic deviations between the average measured and input value of galaxy parameters (see Tables A.3 and A.4). In most cases these deviations are small compared with the estimated statistical (noise) error but for the smallest objects. These systematic deviations may reflect the numeric uncertainties in the PSF deconvolution when R_e is of the order of the size of the PSF core. The FWHM of MICADO PSF in the J , H , and K band is 2.5 , 2.8 , and 3.5 pixel (7.5 , 8.4 and 10.5 mas), respectively. The R_e of the galaxies are listed in Table A.1 and A.2.

According to these simulations, MICADO should be able to provide accurate measurements of the structural and photometric parameters of high-redshift galaxies that are impossible to achieve with current instrumentation. In fact a reliable measurement of the size of the smallest galaxies in our sample ($\lesssim 0''.1$) is beyond the resolution limit of available space and ground-based cameras. For instance, van der Wel et al. (2012) estimated the structural parameters of several high- z galaxies measured from

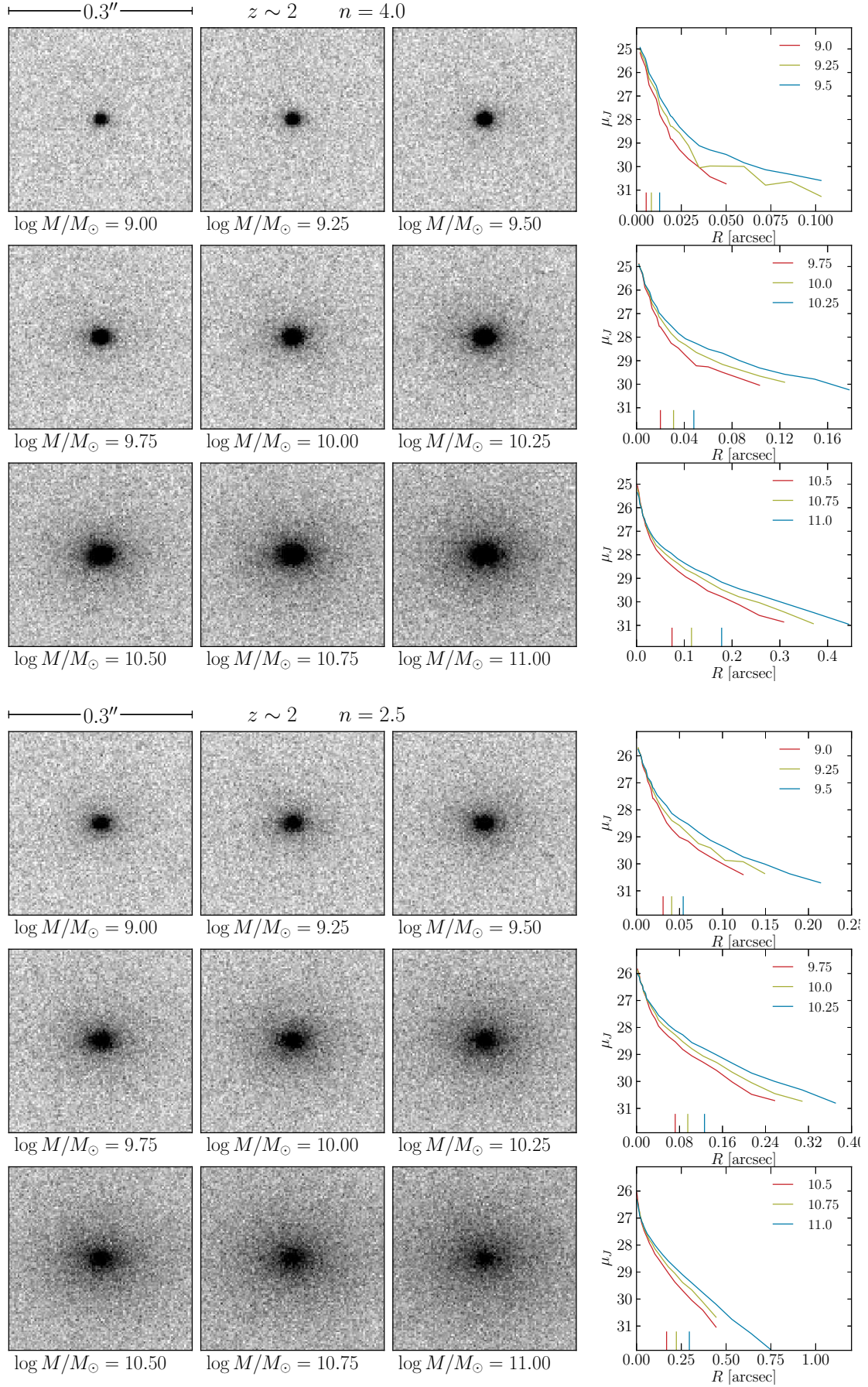


Fig. 2. Central $0.3'' \times 0.3''$ region of J -band images of a sample of simulated $z = 2$ galaxies with Sersic index $n = 4.0$ and 2.5 . The surface brightness profiles are shown in the *right panels*. The small vertical lines show the effective radii of each galaxy.

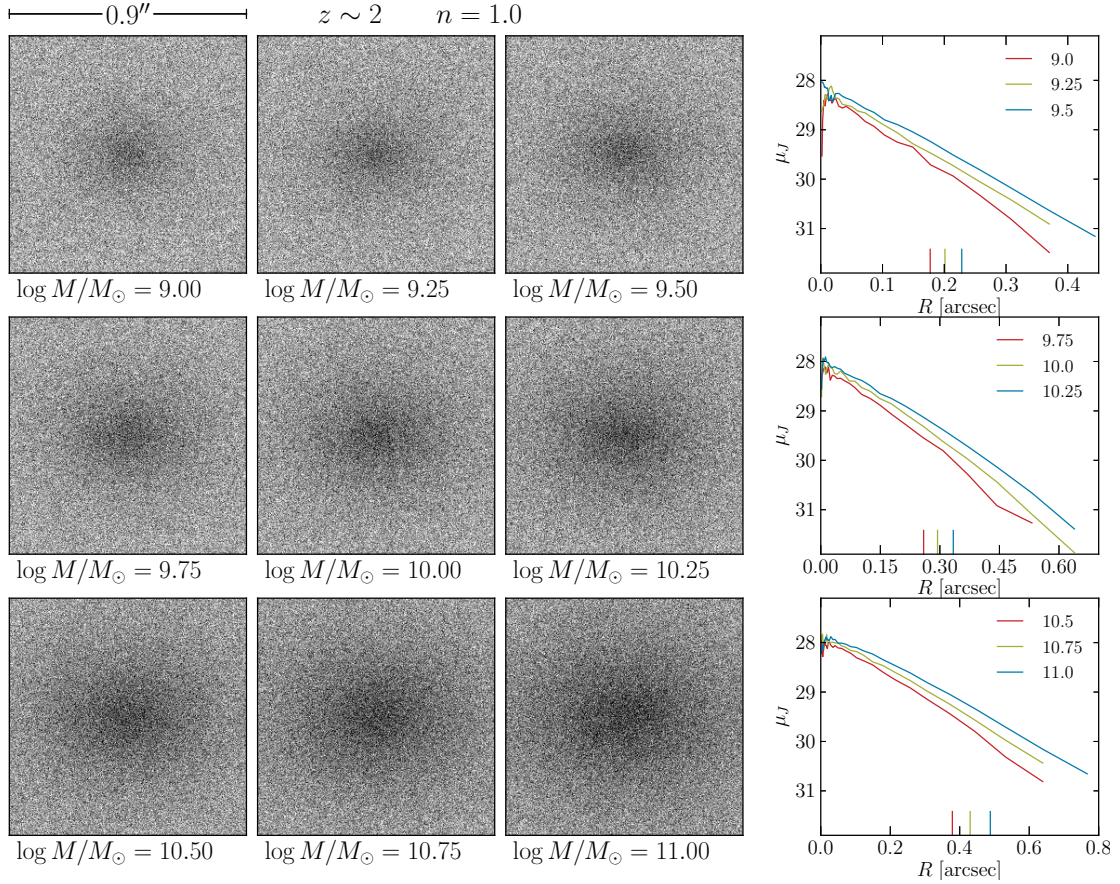


Fig. 3. Central $0.9'' \times 0.9''$ region of J -band images of a sample of simulated $z = 2$ galaxies, with Sersic index $n = 1.0$. The surface brightness profiles are shown in the *right panels*. The small vertical lines show the effective radii of each galaxy.

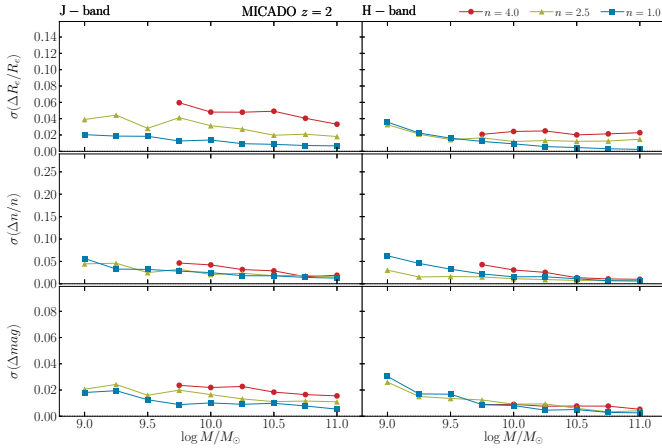


Fig. 4. Accuracy of structural parameters (effective radius, Sersic index, and total magnitude) measurements obtained from MICADO observations of $z = 2$ galaxies with input Sersic indices equal to 1.0 (*blue squares*), 2.5 (*green triangles*), and 4.0 (*red circles*). Results obtained in the J and H bands are shown in the *left* and *right panels*, respectively.

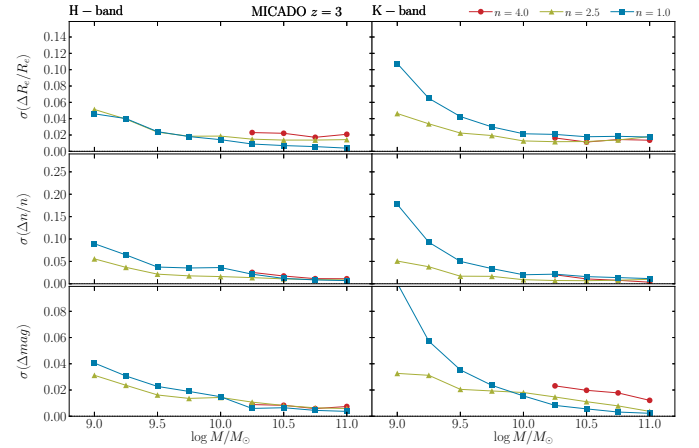


Fig. 5. As in Fig. 5 for H - and K -band simulations of $z = 3$ galaxies.

HST WFC3 IR observations of the CANDELS programme and found that an accuracy of $\sim 10\%$ is only obtained for objects brighter than $H = 23$ mag. In order to properly measure the structure of fainter galaxies that represent the dominant fraction of the population, it is mandatory to use near-IR instrumentation with higher spatial resolution as that expected from ELTs.

In conclusion MICADO will provide very accurate measurements of the structural parameters of high-redshift galaxies for all galaxies with an angular size larger than 20 mas (corresponding to ~ 0.15 kpc). Even for galaxies with steep profiles ($n \sim 4$) and very low mass, down to $10^9 M_\odot$, it will be possible to measure their effective radii and morphology (Sersic index) with uncertainty of about 10–20%.

3.2. Effects of PSF spatial variations

The simulations described above assume ideal conditions. Galaxies were simulated at the centre of the MAORY FoV and GALFIT measurements were carried out using the simulated image of a star located at same the position in the field as a PSF model. Likely the PSF of real observations will be affected by spatial and time variations. As a consequence, the PSF that will be used to analyse the galaxies profiles, will somehow be different from the PSF at the position of the galaxy.

To assess the uncertainty on the determination of structural parameters induced by PSF variations, one should explore a vast parameter space, e.g. considering changes of Strehl ratio, variation of the elongation of the PSF core, and temporal and spatial variations. At the present stage of the design of the instruments it is not possible to properly investigate the impact of all these effects. This exercise is beyond the scope of this paper. Nevertheless to shed some light on the impact of PSF variation on this science case, we consider the specific circumstance in which the PSF model used in GALFIT to deconvolve the galaxy radial surface brightness profile is not exactly the same as that used to generate the galaxy image with AETC. This test was carried out with three different MAORY PSFs that were calculated for positions with an offset from the centre of the FOV of 5'', 10'', and 20'' in both X and Y directions. We refer to these as PSF05, PSF10, and PSF20.

When using PSF05 and PSF10, we retrieved the correct R_e with systematic uncertainties of the order of 5–10%, while using the PSF20 the uncertainties turn out of 20–30%. The error on the magnitude is always ≤ 0.1 mag, while that on the Sersic index depends on the size of the galaxies. The systematic error in the measurements can be as high as 40% for the smallest objects, but is of the order of 10% for galaxies with $R_e > 10$ pixels (40 mas).

We conclude that for science cases aiming at measuring structural parameters of relatively large galaxies ($R_e \sim 40$ mas) with an accuracy of $\sim 10\%$, PSF time and spatial variations would not be a critical issue. Particular care and/or dedicated observations would instead be required to perform extremely accurate measurements of very compact galaxies.

3.3. Comparison with NIRCcam at the JWST

Before ELTs become operative, the most relevant future facility for the study of high-redshift galaxies is the NIRCcam at the JWST. It is of interest thus to compare the expected performances of NIRCcam at the JWST in the determinations of the structural parameters of high-redshift galaxies with those expected for MICADO. To this aim, we considered the galaxies at $z = 2$ presented in the previous sections. We did not take into account galaxies with $n = 4.0$ and $M < 10^{10} M_\odot$ because their R_e (~ 30 mas) is smaller than 1 pixel and it would therefore be beyond the limits of NIRCcam spatial resolution⁴. All simulations were carried out with AETC using the NIRCcam specifications given in the NIRCcam Exposure Time Calculator⁵.

For these data we performed the same analysis as for MICADO simulations. The results are shown in Fig. 6. For galaxies with $n = 1$ the accuracy in the measurements in the bands J and H for R_e and n are $< 5\%$ over the whole range of considered parameters, and of 2–3% for the total magnitude. These are star-forming galaxies that have R_e in the range 200–500 mas

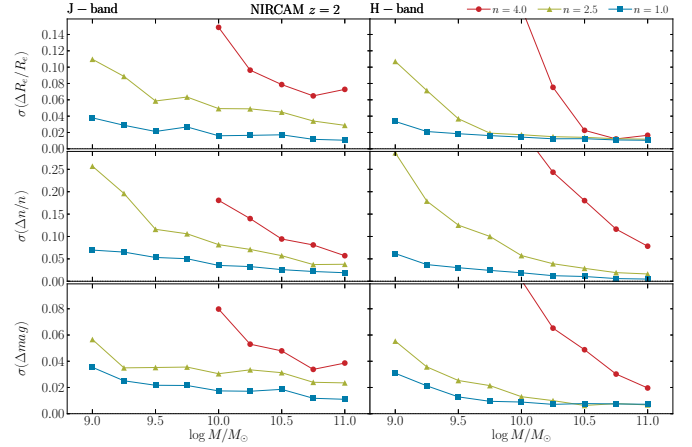


Fig. 6. As in Fig 4 for simulations of NIRCcam at the JWST observations of J - and H -band galaxies at $z = 2$.

and thus their global properties could be derived with similar accuracy by JWST and E-ELT (see Figs. 4 and 6). Conversely, a significant difference between MICADO and NIRCcam accuracy is found for galaxies with $n = 2.5$ and $n = 4.0$ at $z = 2$. In the case of MICADO for all the simulated galaxies the accuracy of R_e and n remains better than 5%, while we found uncertainties in the range 10–25% for NIRCcam observations. The accuracy is particularly poor for galaxies with $n = 4$. This is because the R_e of these galaxies is smaller than ~ 2 pixels in NIRCcam images (see Table A.1). There is about a factor of 2 worse accuracy for galaxies with $n = 4$ compared to those with $n = 2.5$. Only for the most massive and largest galaxies ($M > 10^{10.5} M_\odot$ and $R_e > 100$ mas) the structural parameters are recovered with an accuracy better than 5%, but these represent only a small fraction of the galaxy population. The estimated accuracy appears worse for H -band observations with respect to J -band observations.

3.4. Colour gradients

In Sect. 3.1 we showed that with E-ELTs observations it will be possible to characterise the properties of distant galaxies with an accuracy of a few percent. The comparison of high quality images of these galaxies in different bands offers the opportunity to investigate the trend of the colour of galaxies as a function of distance from the centre. Colour gradients, and their dependence on redshift, can be used to test models of galaxy formation (Saglia et al. 2000; Gargiulo et al. 2012). Decoding a colour gradient in terms of an age or a metallicity gradient depends on the age and metallicity of the stellar population. For relatively young stellar populations ($\lesssim 3$ Gyr), as appropriate for high-redshift galaxies, $\Delta(U - V)/\Delta(\log(\text{age})) \sim 1$ mag/dex at metallicities around solar. The dependence of the $U - V$ colour on metallicity is lower, $\Delta(U - V)/\Delta[\text{Fe}/\text{H}] \sim 0.3$ mag/dex, for stellar populations of 1 to 3 Gyr of age, and metallicities between $0.1 Z_\odot$ and $2 Z_\odot$. Therefore, a $U - V$ colour gradient of 0.1 magnitude may correspond to a variation of $\sim 25\%$ in age or of 0.3 dex in metallicity. The interpretation of colour gradients in terms of the characteristics of the parent stellar population is complicated by various effects, including the well-known, age-metallicity degeneracy. It is however worth assessing the accuracy with which it will be possible to measure the colour gradients of high-redshift galaxies, whose study will provide the means to investigate systematic variations of the stellar populations.

⁴ NIRCcam pixel scale is 31.7 mas/pixels, i.e. ~ 10 times larger than that of MICADO.

⁵ version 1.6 <http://jwstetc.stsci.edu/etc/>

In these simulations we used the same input structural parameters (R_e and n) in the two photometric bands for all galaxies. Therefore, our simulated galaxies have colour gradients that are equal to zero by construction. The errors in the output structural parameters introduce a spurious colour gradient, which can be considered an error on the colour gradient measured from the simulated images. Since the accuracy of the derived colour profile does not strongly depend on the actual value of the colour gradient, but rather on the total magnitude of the galaxy and its size, the uncertainties derived from the analysis of galaxies with zero colour gradient are also valid for galaxies with non-zero colour gradient.

We computed the rest-frame $U - V$ colour profile as the difference between the best-fit Sersic model in J - and H -band for galaxies at $z = 2$ and H - and K -band at $z = 3$ for each simulated galaxy. The gradient was then calculated by fitting a linear relation to the colour profile (in the $\mu_U - \mu_V$ versus $\log R$ plane) in the region $0.1 < R/R_e < 1.0$. We evaluated the mean and standard deviation values of the distributions of the 50 gradients that we computed for the 50 simulations of each template galaxy in each band. The results are reported in Tables A.5 and A.6. As in the case of the structural parameters, we evaluated the overall uncertainty in the colour gradient as the sum in quadrature of the systematic error and of the random error (see Fig. 7). The recovered colour gradients for galaxies with $n = 1.0$ and 2.5 are all compatible, within the uncertainties, with the input value (zero) for both $z = 2$ and $z = 3$ galaxies.

At $z = 2$, the uncertainties in the colour gradient measurements are of the order of $\lesssim 0.05$ mag/dex for galaxies with $M \gtrsim 10^{10} M_\odot$ and ~ 0.10 mag/dex for the smallest galaxies with $M = 10^9 M_\odot$ (upper panel in Fig. 7). The results are essentially the same for galaxies at $z = 3$ with $n = 4.0$ and 2.5. The uncertainties are larger for late-type galaxies ($n = 1.0$). They are of the order of ~ 0.10 mag/dex for galaxies with $M \gtrsim 10^{10} M_\odot$ and up to ~ 0.35 mag/dex for $M = 10^9 M_\odot$ galaxies. This is mainly because of the lower accuracy of the structural parameters derived from K -band images (see Fig. 5).

In summary we found that MICADO images of high- z galaxies can be used to measure their colour gradients in the inner galactic regions ($R < R_e$) with an accuracy of 0.1 mag/dex in all galaxies with $M \gtrsim 10^9 M_\odot$ at $z = 2$ and with $M \gtrsim 10^{10} M_\odot$ at $z = 3$. A similar accuracy is also expected for early-type galaxies ($n \geq 2.5$) at $z = 3$ and $M \gtrsim 10^9 M_\odot$. In the case of late-type dwarf galaxies at $z = 3$ we instead expect an accuracy of about 0.3 mag/dex.

3.5. Simulated high- z galaxies using templates

While for early-type passive galaxies the Sersic law provides an accurate description of the surface brightness profile, late-type star-forming galaxies have a much more complex morphology. Besides the exponential stellar disk, in late-type galaxies there are often also a number of conspicuous substructures, such as spiral arms, clumpy star-forming regions, and dust lanes. The study of these features offers further important clues to understand the processes of galaxy formation and evolution. In this section we complement the description of the capabilities of ELTs and JWST to characterise the morphology and structural parameters of galaxies with simulations of observations of galaxies with a more complex morphology. Simulations of observations of high- z galaxies using HARMONI, the future integral-field spectrograph for the E-ELT, was presented by Kendrew et al. (2016).

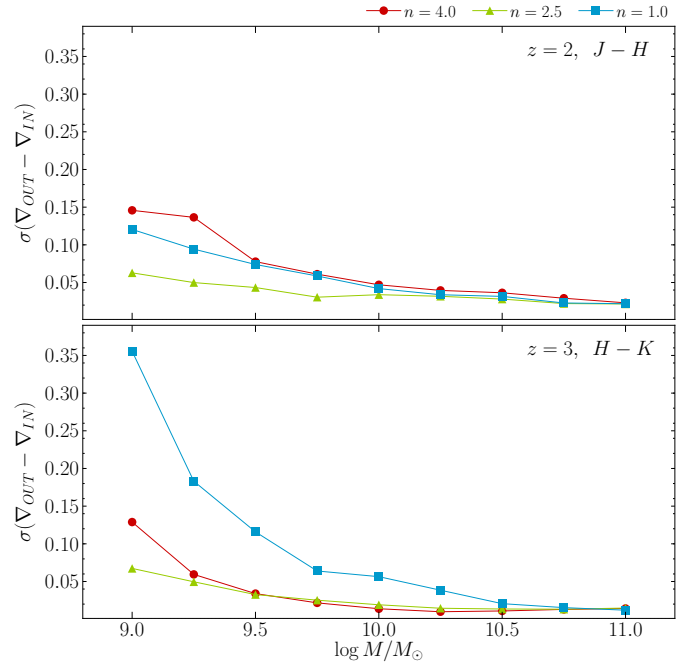


Fig. 7. Uncertainty in the colour gradient for galaxies of different stellar mass and Sersic index, as obtained from simulations of MICADO observations of high-redshift galaxies. The $J - H$ and $H - K$ colours correspond to rest-frame $U - V$ at redshift $z = 2$ (top panel) and $z = 3$ (bottom panel).

These kinds of simulations are of particular interest when studying galaxies at $z \approx 2-3$ because these redshifts correspond to the epoch of maximum cosmic star formation rate (Madau & Dickinson 2014), when the fraction of star-forming late-type galaxies and merging galaxies was much higher than at the present epoch.

We performed simulated observations of high- z galaxies with template images obtained from high-resolution observations of nearby galaxies. To this aim, we looked for Advance Camera for Survey (ACS) and/or WFC3 observations of galaxies with different morphologies in the HST archive. We selected observations in photometric bands that roughly correspond to J and H (H and K) when redshifted at $z \sim 2$ (~ 3) for three different objects: (i) images in the filters $F435W$ and $F606W$ of NGC 6217 ($z = 0.004$), a star-forming barred spiral galaxy; (ii) image in filter $F435W$ of UGC 9618 ($z = 0.033$), a pair of gas-rich galaxies (the first is a face-on spiral and the second is a edge-on galaxy with a dense dust lane) in the early stage of interaction; and (iii) images in filters $F475W$ and $F625W$ of ARP 142 ($z = 0.023$), which is a violent merger of an elliptical galaxy with a disrupting gas-rich galaxy. We removed all foreground stars, background galaxies, cosmic rays, and artefacts from the original HST images. We then used AETC to produce MICADO and JWST simulated observations (using same prescriptions described in Sect. 2) with a total integration time of three hours. The total flux and angular size of the templates were rescaled to match the magnitude and size of galaxies at redshift 2 and 3, using the values in Fig. 1 as a reference. These simulated observations are shown in Figs. 8 and 9. Each set of three figures shows the original template the MICADO image and the NIRCcam image. We applied a box car filter with size of 3 pixels to the MICADO images to increase the signal-to-noise ratio to enhance the low surface brightness features.

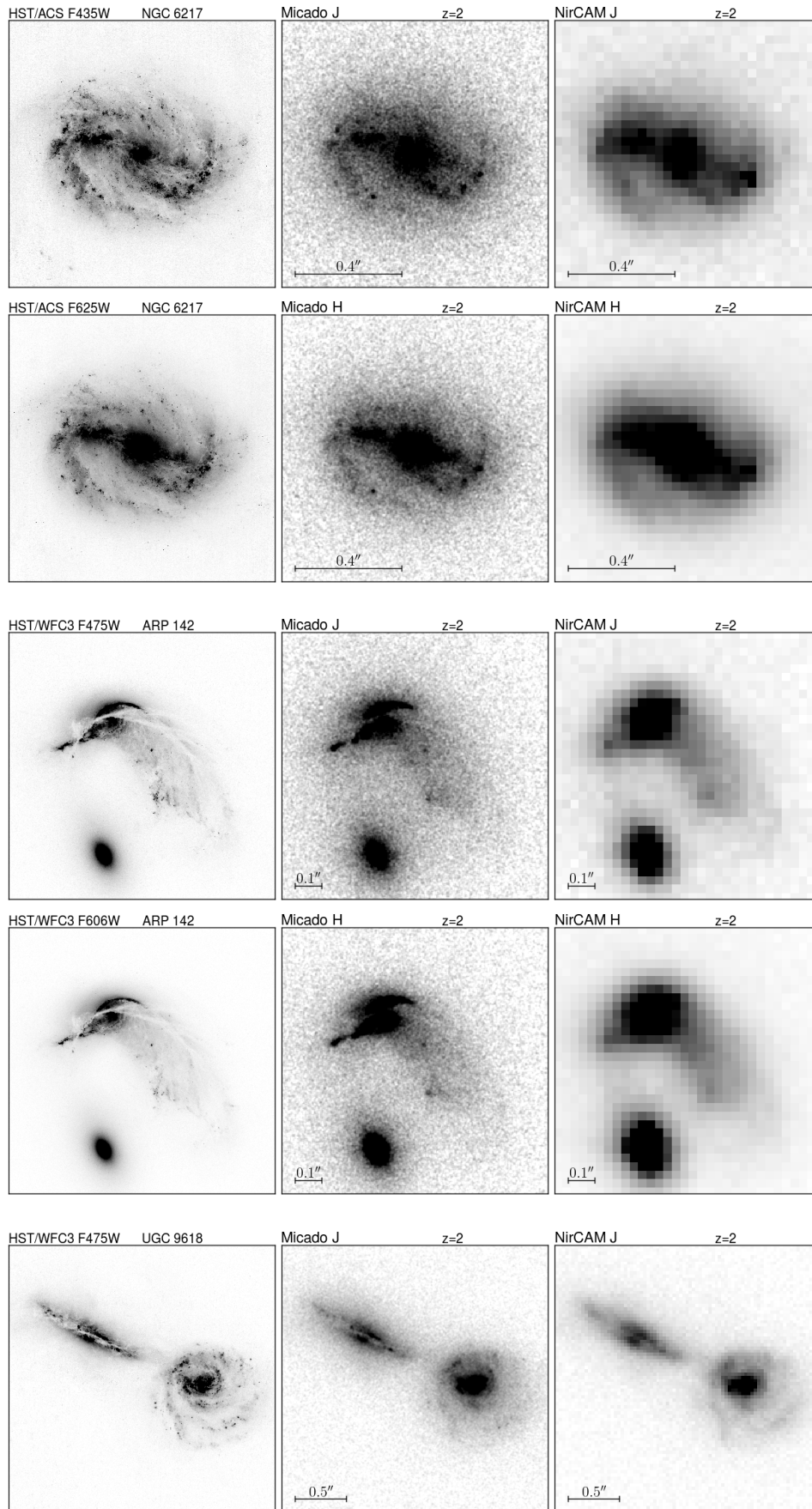


Fig. 8. Simulations of MICADO (*central panels*) and NIRCAM (*right panels*) *J*- and *H*-band observations of galaxies at $z \sim 2$ obtained using HST observations of nearby galaxies as templates (*left panels*).

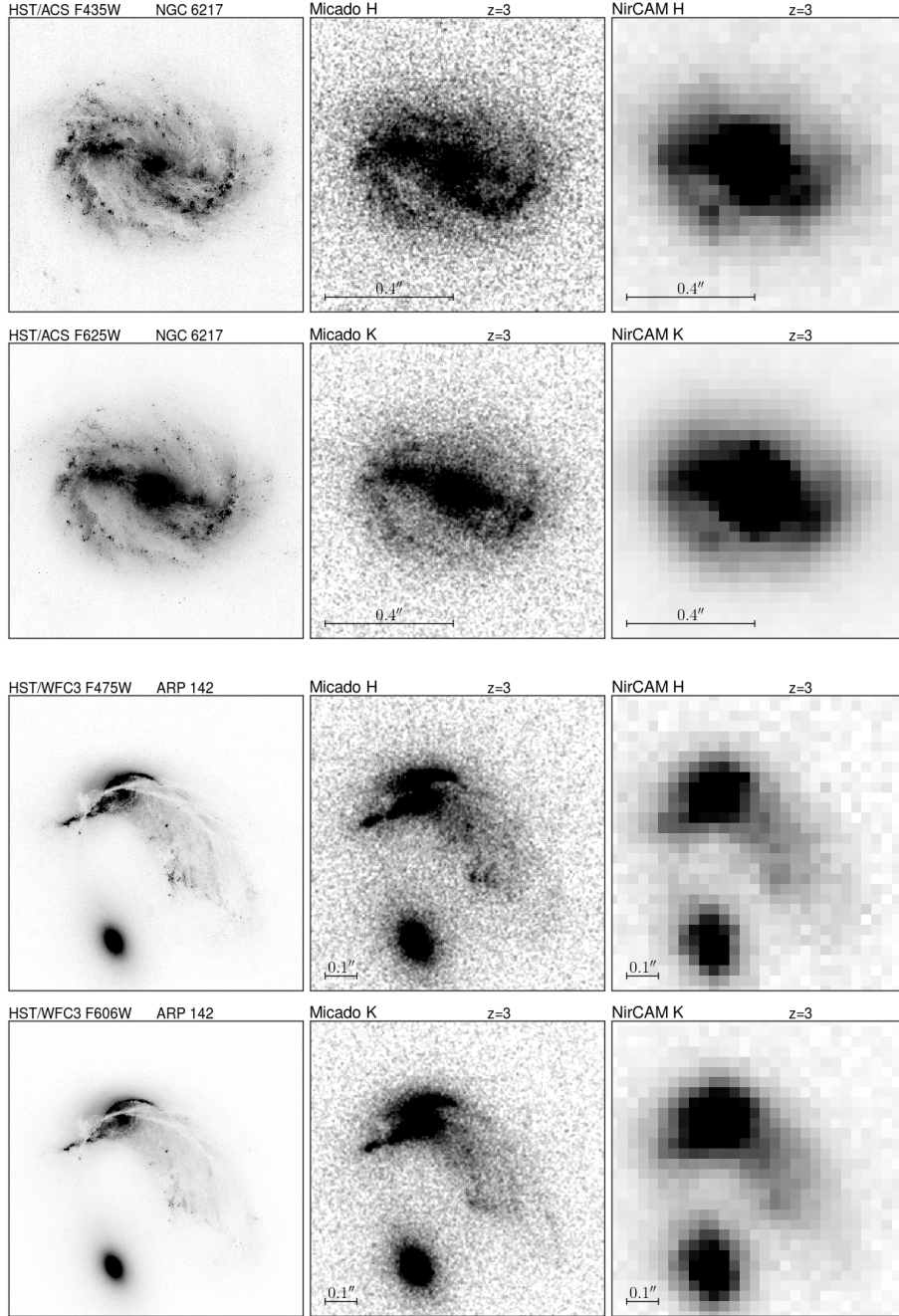


Fig. 9. Simulations of MICADO (*central panels*) and NIRCAM (*right panels*) H - and K -band observations of galaxies at $z \sim 3$ obtained using HST observations of nearby galaxies as templates (*left panels*.)

Since the spatial resolution of MICADO is a factor ~ 6 higher than that of NIRCAM, these small substructures are much better defined in MICADO images than in NIRCAM images. For example, JWST could barely resolve the bar and spiral arms of a late-type galaxy with $R_e \sim 0''.3$, while a 40-m class ground-based ELT would also be able to resolve the brightest star-forming regions; see e.g. the simulations obtained using NGC 6217 and UGC 9618 as a template Figs. 8 and 9. ELTs would also be able to detect dense dust lanes in galaxies up to redshift 2 or 3. The third example was obtained using the violent merger ARP 142 and shows that, in spite of the significant lower background for JWST observations in H and K bands, the combination of higher resolution and larger sensitivity (39 m aperture compared with 6.5 m) of E-ELT allow MICADO to detect the low surface

brightness regions (e.g. the tail of the disrupting late-type galaxy in ARP 142) slightly better than NIRCAM and also to distinguish the fine (~ 50 mas) substructures (see Figs. 8 and 9).

4. Summary and conclusions

In this paper we presented a detailed analysis of the expected performances of next-generation ELTs in the characterisation of the properties of high- z galaxies. We evaluated the accuracy in the measurements of the structural and photometric parameters that will be obtained from future observations using an extensive set of simulated observations. As a reference, we used the specifications of the MICADO camera to be mounted at the E-ELT and the NIRCAM at the JWST. The extraordinary large

diameter of the E-ELT will provide imaging of high-redshift galaxies with unprecedented spatial resolution.

Our results confirm that MICADO will provide extremely accurate measurements of the structural parameters of high-redshift galaxies; systematic uncertainties in the measurements of structural parameters are expected to be negligible for galaxies with effective radii larger than ~ 20 mas. The overall uncertainties in the measurements of the structural parameters of late-type galaxies result to be smaller than 5% and the uncertainties in the total magnitude of a few hundredths of magnitude, even for the smallest simulated galaxies ($M = 10^9 M_\odot$, $H \sim 24.5$ mag). For early-type galaxies that are more compact and have a steeper profile ($n = 4$) than late-type galaxies, we found that MICADO would provide measurements of the effective radius and the Seric index with uncertainties of just 10–20% even for the smallest and faintest galaxies considered in our study ($M = 10^9 M_\odot$, $H \sim 26.5$ mag). These results confirm that MICADO observations will represent a real breakthrough as they will facilitate results far beyond the capabilities of present-day instrumentation. Today, this accuracy is obtained with the HST for galaxies ~ 3 mag brighter and at least 10 times more massive and/or bigger (see e.g. van der Wel et al. 2014).

We also estimate that, from ELTs observations, it will be possible to obtain reliable measures of colour gradients as small as 0.3 mag/dex in galaxies at $z = 3$. Therefore it will be possible to study the population gradients in high-redshift galaxies. This will represent a fundamental step to understand the assembly history and physical processes regulating the formation, the growth and, evolution of the galaxies. This study is nowadays possible only for nearby galaxies; the advent of the ELTs will make it possible to extend these studies at $z = 2$ and 3, probing galaxies at the epoch in which the star formation rate density peaked ($z \simeq 2$; e.g. Madau & Dickinson 2014) and beyond.

We also provided a quantitative estimate of the performances expected for the JWST. We found that NIRCcam will provide excellent measurements for late-type galaxies down to $M \sim 10^{10} M_\odot$ at $z = 2$. The size of low-mass early-type galaxies ($M \lesssim 10^{10} M_\odot$) at $z = 3$ would be of the order of (or even smaller than) the spatial resolution of the JWST and therefore it would be extremely difficult to derive reliable measurements of their spatial and photometric parameters. The first opportunity to explore the details of the structure of distant compact galaxies, or the very inner region of galaxies at lower redshift, will be offered by the advent in the next decade of the imagers at ground-based extremely large telescopes and, in particular, of MICADO at the E-ELT.

We finally performed simulations of high- z galaxies using high-resolution HST images of galaxies at low redshift. These simulations manifest how the combined capabilities of excellent angular resolution and sensitivity will allow us to investigate in great detail the small substructures (spiral arms, clumpy star-forming regions, dust lanes, etc.) of distant galaxies that could not be investigated by any other present or actually planned ground- or space-based facilities.

Acknowledgements. We acknowledge support of INAF and MIUR through the grant *Progetto premiale T-REX*.

References

- Brammer, G. B., van Dokkum, P. G., Franx, M., et al. 2012, *ApJS*, **200**, 13
 Buitrago, F., Trujillo, I., Conselice, C. J., et al. 2008, *ApJ*, **687**, L61
 Ciotti, L. 1991, *A&A*, **249**, 99
 Daddi, E., Renzini, A., Pirzkal, N., et al. 2005, *ApJ*, **626**, 680
 Dalcanton, J. J., Spergel, D. N., & Summers, F. J. 1997, *ApJ*, **482**, 659
 Davies, R., Ageorges, N., Barl, L., et al. 2010, in Ground-based and Airborne Instrumentation for Astronomy III, eds. I. S. McLean, S. K. Ramsay, & H. Takami, *Proc. SPIE*, **7735**, 77352
 Diolaiti, E., Conan, J.-M., Foppiani, I., et al. 2010, in Adaptive Optics Systems II, eds. B. L. Ellerbroek, M. Hart, N. Hubin, & P. L. Wizinowich, *Proc. SPIE*, **7736**, 77360
 Falomo, R., Fantinel, D., & Uslenghi, M. 2011, in Applications of Digital Image Processing XXXIV, ed. A. G. Tescher, *Proc. SPIE*, **8135**, 813523
 Gargiulo, A., Saracco, P., & Longhetti, M. 2011, *MNRAS*, **412**, 1804
 Gargiulo, A., Saracco, P., Longhetti, M., La Barbera, F., & Tamburri, S. 2012, *MNRAS*, **425**, 2698
 Gullieuszik, M., Greggio, L., Falomo, R., Schreiber, L., & Uslenghi, M. 2014, *A&A*, **568**, A89
 Kelvin, L. S., Driver, S. P., Robotham, A. S. G., et al. 2012, *MNRAS*, **421**, 1007
 Kendrew, S., Zieleniewski, S., Houghton, R. C. W., et al. 2016, *MNRAS*, **458**, 2405
 Kennedy, R., Bamford, S. P., Baldry, I., et al. 2015, *MNRAS*, **454**, 806
 Kobayashi, C. 2004, *MNRAS*, **347**, 740
 Madau, P., & Dickinson, M. 2014, *ARA&A*, **52**, 415
 Mo, H. J., Mao, S., & White, S. D. M. 1998, *MNRAS*, **295**, 319
 Ono, Y., Ouchi, M., Curtis-Lake, E., et al. 2013, *ApJ*, **777**, 155
 Peng, C. Y., Ho, L. C., Impey, C. D., & Rix, H.-W. 2002, *AJ*, **124**, 266
 Saglia, R. P., Maraston, C., Greggio, L., Bender, R., & Ziegler, B. 2000, *A&A*, **360**, 911
 Tamura, N., Kobayashi, C., Arimoto, N., Kodama, T., & Ohta, K. 2000, *AJ*, **119**, 2134
 Trujillo, I., Feulner, G., Goranova, Y., et al. 2006, *MNRAS*, **373**, L36
 van der Wel, A., Bell, E. F., Häußler, B., et al. 2012, *ApJS*, **203**, 24
 van der Wel, A., Franx, M., van Dokkum, P. G., et al. 2014, *ApJ*, **788**, 28
 Vulcani, B., Bamford, S. P., Häußler, B., et al. 2014, *MNRAS*, **441**, 1340

Appendix A: Supplementary tables and figures**Table A.1.** Effective radius, J - and H -band magnitudes adopted for the template galaxies at $z = 2$.

$\log M/M_{\odot}$	R_e [kpc]	R_e ["]	J	H
$n = 1.0$				
9.00	1.5005	0.1772	25.000	25.000
9.25	1.7030	0.2011	24.726	24.538
9.50	1.9330	0.2283	24.450	24.075
9.75	2.1939	0.2591	24.176	23.613
10.00	2.4902	0.2941	23.900	23.150
10.25	2.8264	0.3338	23.626	22.688
10.50	3.2079	0.3788	23.350	22.225
10.75	3.6410	0.4300	23.076	21.763
11.00	4.1326	0.4880	22.800	21.300
$n = 2.5$				
9.00	0.2615	0.0309	26.125	25.500
9.25	0.3467	0.0409	25.788	25.038
9.50	0.4597	0.0543	25.450	24.575
9.75	0.6095	0.0720	25.113	24.113
10.00	0.8082	0.0954	24.775	23.650
10.25	1.0715	0.1265	24.438	23.188
10.50	1.4207	0.1678	24.100	22.725
10.75	1.8837	0.2224	23.763	22.263
11.00	2.4975	0.2949	23.425	21.800
$n = 4.0$				
9.00	0.0456	0.0054	27.250	26.000
9.25	0.0706	0.0083	26.850	25.538
9.50	0.1093	0.0129	26.450	25.075
9.75	0.1693	0.0200	26.050	24.613
10.00	0.2623	0.0310	25.650	24.150
10.25	0.4062	0.0480	25.250	23.688
10.50	0.6292	0.0743	24.850	23.225
10.75	0.9745	0.1151	24.450	22.763
11.00	1.5093	0.1782	24.050	22.300

Table A.2. Effective radius, H - and K -band magnitudes adopted for the template galaxies at $z = 3$.

$\log M/M_{\odot}$	R_e [kpc]	R_e ["]	H	K
$n = 1.0$				
9.00	1.2604	0.1634	25.500	25.800
9.25	1.4306	0.1855	25.038	25.150
9.50	1.6237	0.2106	24.575	24.500
9.75	1.8430	0.2390	24.113	23.850
10.00	2.0918	0.2712	23.650	23.200
10.25	2.3742	0.3079	23.188	22.550
10.50	2.6947	0.3494	22.725	21.900
10.75	3.0585	0.3966	22.263	21.250
11.00	3.4715	0.4502	21.800	20.600
$n = 2.5$				
9.00	0.2082	0.0270	26.000	25.675
9.25	0.2752	0.0357	25.538	25.088
9.50	0.3639	0.0472	25.075	24.500
9.75	0.4811	0.0624	24.613	23.913
10.00	0.6360	0.0825	24.150	23.325
10.25	0.8409	0.1090	23.688	22.738
10.50	1.1117	0.1442	23.225	22.150
10.75	1.4697	0.1906	22.763	21.563
11.00	1.9430	0.2520	22.300	20.975
$n = 4.0$				
9.00	0.0344	0.0045	26.500	25.550
9.25	0.0530	0.0069	26.038	25.026
9.50	0.0816	0.0106	25.575	24.500
9.75	0.1256	0.0163	25.113	23.976
10.00	0.1934	0.0251	24.650	23.450
10.25	0.2978	0.0386	24.188	22.926
10.50	0.4586	0.0595	23.725	22.400
10.75	0.7062	0.0916	23.263	21.876
11.00	1.0875	0.1410	22.800	21.350

Table A.3. Mean values and dispersion of the distribution of residuals in measured effective radius, Sersic index, and magnitude in J - and H -band simulations of $z = 2$ galaxies.

$\log M/M_{\odot}$	$\Delta n/n^J$ [%]	$\Delta R_e/R_e^J$ [%]	ΔJ	$\Delta n/n^H$ [%]	$\Delta R_e/R_e^H$ [%]	ΔH
$n = 1.0$						
9.00	1.2 ± 5.5	0.2 ± 2.0	-0.00 ± 0.02	-1.1 ± 6.2	-0.3 ± 3.6	-0.00 ± 0.03
9.25	0.1 ± 3.3	0.2 ± 1.8	-0.01 ± 0.02	-0.6 ± 4.5	0.4 ± 2.2	0.00 ± 0.02
9.50	-0.2 ± 3.2	0.4 ± 1.8	-0.00 ± 0.01	-0.3 ± 3.3	0.1 ± 1.6	-0.00 ± 0.02
9.75	-0.3 ± 2.8	-0.4 ± 1.2	0.00 ± 0.01	-1.0 ± 1.9	0.1 ± 1.2	-0.00 ± 0.01
10.00	-0.7 ± 2.4	-0.1 ± 1.4	0.00 ± 0.01	-0.6 ± 1.4	-0.0 ± 0.9	0.00 ± 0.01
10.25	0.0 ± 1.8	0.1 ± 0.9	-0.00 ± 0.01	-0.9 ± 1.3	-0.2 ± 0.5	0.00 ± 0.00
10.50	-0.6 ± 1.7	-0.2 ± 0.8	0.00 ± 0.01	-0.4 ± 1.0	0.0 ± 0.5	0.00 ± 0.01
10.75	0.3 ± 1.4	0.0 ± 0.7	0.00 ± 0.01	-0.3 ± 0.6	0.0 ± 0.3	0.00 ± 0.00
11.00	-0.1 ± 1.3	0.1 ± 0.7	0.00 ± 0.01	-0.4 ± 0.5	-0.0 ± 0.2	0.00 ± 0.00
$n = 2.5$						
9.00	0.2 ± 4.4	-1.9 ± 3.4	-0.01 ± 0.02	0.3 ± 3.0	0.4 ± 3.3	-0.01 ± 0.02
9.25	-1.3 ± 4.4	-2.5 ± 3.6	-0.01 ± 0.02	-0.6 ± 1.4	-0.7 ± 2.0	-0.01 ± 0.01
9.50	0.4 ± 2.5	-0.9 ± 2.7	-0.01 ± 0.01	-0.2 ± 1.6	-0.3 ± 1.4	-0.01 ± 0.01
9.75	0.3 ± 3.2	-1.2 ± 3.9	-0.01 ± 0.02	-0.3 ± 1.5	-0.4 ± 1.6	-0.01 ± 0.01
10.00	0.3 ± 2.0	-1.3 ± 2.8	-0.00 ± 0.02	-0.4 ± 1.1	-0.3 ± 1.2	-0.01 ± 0.01
10.25	0.5 ± 2.3	-1.0 ± 2.5	-0.00 ± 0.01	-0.2 ± 0.9	-0.2 ± 1.3	-0.01 ± 0.01
10.50	0.4 ± 1.8	-0.9 ± 1.8	0.00 ± 0.01	-0.5 ± 0.6	-0.7 ± 1.0	-0.00 ± 0.00
10.75	0.1 ± 1.9	-1.1 ± 1.8	-0.00 ± 0.01	-0.6 ± 0.4	-1.1 ± 0.6	0.00 ± 0.00
11.00	0.2 ± 1.5	-0.8 ± 1.6	0.00 ± 0.01	-0.7 ± 0.4	-1.4 ± 0.5	0.00 ± 0.00
$n = 4.0$						
9.00	-16.1 ± 8.2	-3.7 ± 5.6	0.05 ± 0.03	-14.9 ± 3.4	4.6 ± 3.1	0.03 ± 0.01
9.25	-1.7 ± 9.5	0.0 ± 6.2	0.00 ± 0.03	-9.3 ± 2.2	1.5 ± 1.8	0.01 ± 0.01
9.50	-1.8 ± 5.3	-1.5 ± 5.7	0.00 ± 0.03	-6.8 ± 2.0	-0.5 ± 1.8	0.01 ± 0.01
9.75	-1.6 ± 4.3	-2.8 ± 5.3	-0.00 ± 0.02	-4.0 ± 1.6	-0.7 ± 1.9	0.00 ± 0.01
10.00	0.4 ± 4.2	-1.6 ± 4.5	-0.01 ± 0.02	-2.8 ± 1.4	-1.5 ± 2.0	0.00 ± 0.01
10.25	-0.7 ± 3.1	-2.7 ± 3.9	-0.00 ± 0.02	-2.3 ± 1.1	-1.7 ± 1.8	0.00 ± 0.01
10.50	1.0 ± 2.7	-2.1 ± 4.5	-0.00 ± 0.02	-1.1 ± 0.8	-1.1 ± 1.7	-0.00 ± 0.01
10.75	0.2 ± 1.6	-2.3 ± 3.4	0.00 ± 0.02	-0.8 ± 0.8	-1.1 ± 1.8	-0.00 ± 0.01
11.00	0.5 ± 1.8	-2.0 ± 2.7	0.00 ± 0.02	-0.9 ± 0.4	-2.0 ± 1.1	0.00 ± 0.01

Table A.4. Mean values and dispersion of the distribution of residuals in measured effective radius, Sersic index, and magnitude in J - and H -band simulations of $z = 3$ galaxies.

$\log M/M_{\odot}$	$\Delta n/n^H$ [%]	$\Delta R_e/R_e^H$ [%]	ΔH	$\Delta n/n^K$ [%]	$\Delta R_e/R_e^K$ [%]	ΔK
$n = 1.0$						
9.00	-0.2 ± 8.9	1.1 ± 4.5	-0.02 ± 0.04	-6.8 ± 16.4	-5.4 ± 9.3	0.06 ± 0.08
9.25	-3.7 ± 5.3	-1.7 ± 3.6	0.01 ± 0.03	1.0 ± 9.2	-0.0 ± 6.5	0.01 ± 0.06
9.50	0.4 ± 3.7	0.4 ± 2.4	-0.01 ± 0.02	0.2 ± 5.0	2.1 ± 3.7	-0.00 ± 0.04
9.75	-1.8 ± 3.0	-0.4 ± 1.8	0.00 ± 0.02	-1.2 ± 3.2	0.8 ± 2.9	0.01 ± 0.02
10.00	-1.8 ± 3.2	-0.4 ± 1.4	0.00 ± 0.01	0.8 ± 1.9	1.6 ± 1.4	0.01 ± 0.01
10.25	-1.4 ± 1.7	-0.2 ± 0.9	0.00 ± 0.01	1.5 ± 1.5	1.9 ± 0.9	0.00 ± 0.01
10.50	-0.5 ± 1.1	0.1 ± 0.7	0.00 ± 0.01	1.4 ± 0.7	1.7 ± 0.5	0.00 ± 0.01
10.75	-0.3 ± 0.8	-0.1 ± 0.6	0.00 ± 0.00	1.2 ± 0.6	1.8 ± 0.4	-0.00 ± 0.00
11.00	-0.2 ± 0.7	0.1 ± 0.4	0.00 ± 0.00	1.1 ± 0.3	1.7 ± 0.3	-0.00 ± 0.00
$n = 2.5$						
9.00	-1.3 ± 5.4	0.5 ± 5.1	-0.00 ± 0.03	-1.4 ± 4.9	0.3 ± 4.6	0.02 ± 0.03
9.25	-0.7 ± 3.6	0.0 ± 3.9	-0.01 ± 0.02	-1.5 ± 3.5	-1.1 ± 3.2	0.02 ± 0.02
9.50	0.0 ± 2.2	-0.1 ± 2.3	-0.01 ± 0.01	0.1 ± 1.7	-0.2 ± 2.2	0.01 ± 0.01
9.75	-0.1 ± 1.8	0.1 ± 1.9	-0.01 ± 0.01	-0.3 ± 1.6	0.1 ± 1.9	0.02 ± 0.01
10.00	-0.2 ± 1.6	0.3 ± 1.8	-0.01 ± 0.01	-0.1 ± 0.9	-0.4 ± 1.2	0.02 ± 0.01
10.25	-0.5 ± 1.3	-0.4 ± 1.4	-0.01 ± 0.01	-0.1 ± 0.7	0.3 ± 1.1	0.01 ± 0.01
10.50	-0.6 ± 0.9	-0.6 ± 1.2	-0.00 ± 0.01	0.4 ± 0.6	0.8 ± 0.9	0.01 ± 0.00
10.75	-0.6 ± 0.7	-0.8 ± 1.1	-0.00 ± 0.01	0.7 ± 0.3	1.2 ± 0.7	0.01 ± 0.00
11.00	-0.6 ± 0.6	-1.1 ± 0.9	0.00 ± 0.01	1.0 ± 0.3	1.7 ± 0.5	0.00 ± 0.00
$n = 4.0$						
9.00	-17.6 ± 6.2	7.8 ± 3.9	0.04 ± 0.02	-12.1 ± 4.8	7.8 ± 2.3	0.06 ± 0.01
9.25	-11.7 ± 4.2	2.2 ± 3.1	0.03 ± 0.02	-8.8 ± 2.5	2.9 ± 1.3	0.05 ± 0.01
9.50	-8.2 ± 2.6	-0.2 ± 2.6	0.01 ± 0.01	-6.3 ± 2.1	0.7 ± 1.5	0.03 ± 0.01
9.75	-6.2 ± 2.1	-1.5 ± 2.4	0.01 ± 0.01	-3.8 ± 1.3	-0.1 ± 1.4	0.03 ± 0.01
10.00	-3.8 ± 1.8	-1.7 ± 2.2	0.00 ± 0.01	-2.7 ± 0.9	-0.6 ± 1.3	0.02 ± 0.01
10.25	-2.1 ± 1.5	-1.1 ± 2.0	0.00 ± 0.01	-1.8 ± 0.8	-1.1 ± 1.2	0.02 ± 0.00
10.50	-1.4 ± 1.0	-1.2 ± 1.9	-0.00 ± 0.01	-1.0 ± 0.4	-0.5 ± 1.0	0.02 ± 0.00
10.75	-1.0 ± 0.6	-1.1 ± 1.3	-0.00 ± 0.01	-0.6 ± 0.5	-0.4 ± 1.4	0.02 ± 0.00
11.00	-0.9 ± 0.6	-1.6 ± 1.4	-0.00 ± 0.01	0.1 ± 0.3	0.6 ± 1.2	0.01 ± 0.00

Table A.5. Mean values and dispersion of the measured colour gradients measured in $z = 2$ simulated galaxies galaxies.

$\log M/M_{\odot}$	$\nabla(U - V)_{\text{restframe}}$		
	$n = 1.0$ mag/dex	$n = 2.5$ mag/dex	$n = 4.0$ mag/dex
9.00	0.016 ± 0.119	0.018 ± 0.060	0.061 ± 0.133
9.25	0.021 ± 0.092	0.018 ± 0.047	0.104 ± 0.089
9.50	0.004 ± 0.074	0.022 ± 0.037	0.067 ± 0.039
9.75	0.007 ± 0.058	0.009 ± 0.029	0.052 ± 0.032
10.00	-0.002 ± 0.042	0.022 ± 0.026	0.041 ± 0.023
10.25	0.009 ± 0.033	0.020 ± 0.025	0.028 ± 0.028
10.50	-0.003 ± 0.031	0.014 ± 0.025	0.030 ± 0.021
10.75	0.004 ± 0.022	0.009 ± 0.020	0.020 ± 0.021
11.00	0.001 ± 0.022	0.006 ± 0.021	0.013 ± 0.019

Table A.6. Mean values and dispersion of the measured colour gradients measured in $z = 3$ simulated galaxies galaxies.

$\log M/M_{\odot}$	$\nabla(U - V)_{\text{restframe}}$		
	$n = 1.0$ mag/dex	$n = 2.5$ mag/dex	$n = 4.0$ mag/dex
9.00	0.019 ± 0.355	-0.003 ± 0.067	-0.079 ± 0.102
9.25	-0.076 ± 0.166	0.005 ± 0.049	-0.028 ± 0.052
9.50	0.025 ± 0.113	-0.002 ± 0.033	-0.017 ± 0.029
9.75	0.004 ± 0.064	0.001 ± 0.025	-0.013 ± 0.017
10.00	-0.015 ± 0.054	-0.008 ± 0.018	-0.005 ± 0.013
10.25	-0.014 ± 0.036	-0.000 ± 0.015	-0.003 ± 0.009
10.50	-0.008 ± 0.019	0.003 ± 0.013	-0.000 ± 0.011
10.75	0.001 ± 0.015	0.005 ± 0.012	0.003 ± 0.013
11.00	0.004 ± 0.011	0.010 ± 0.011	0.008 ± 0.012

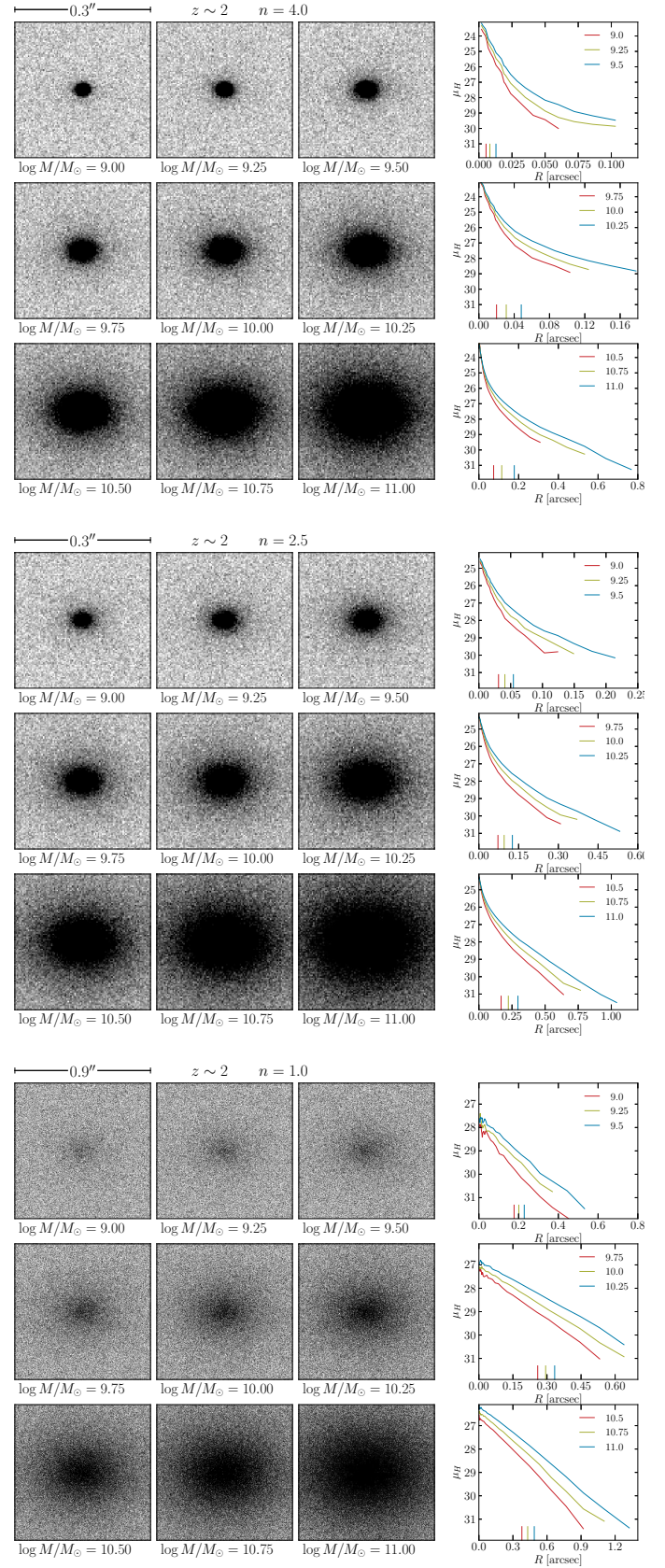


Fig. A.1. As in 2 for H -band images of $z = 2$ galaxies.

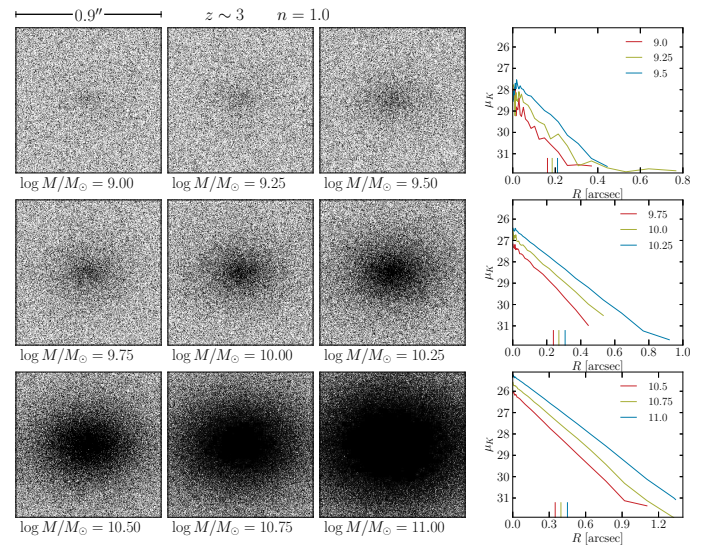
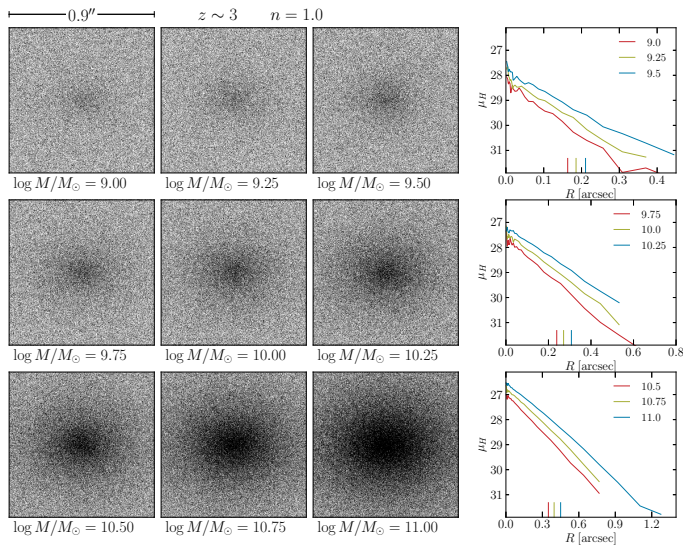
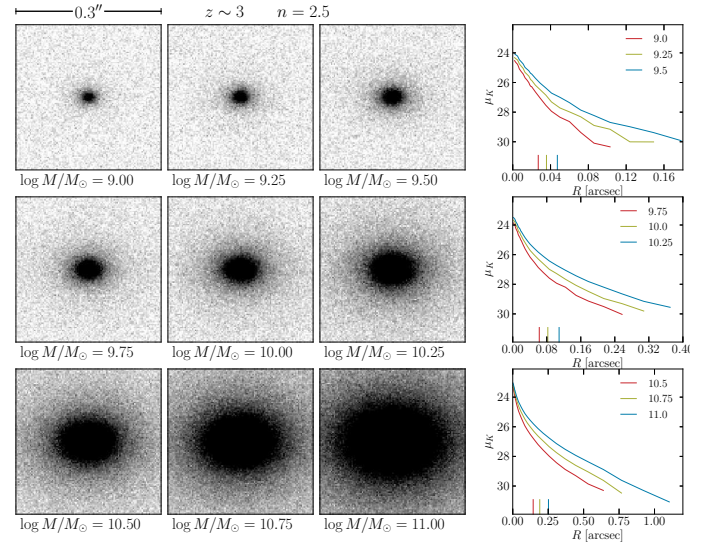
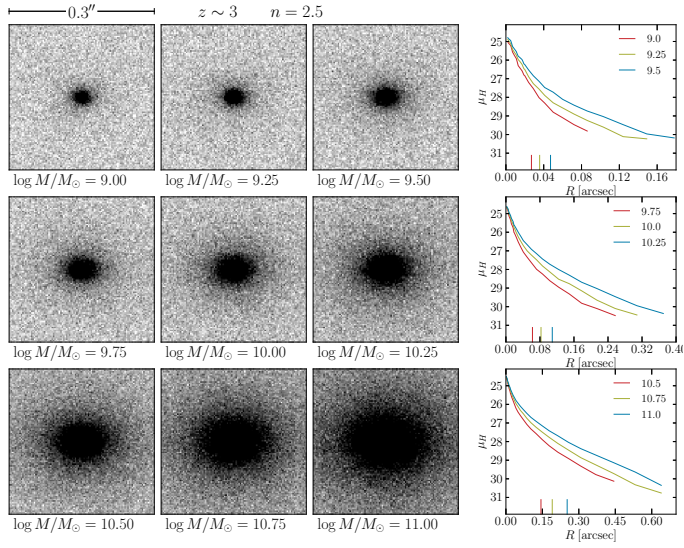
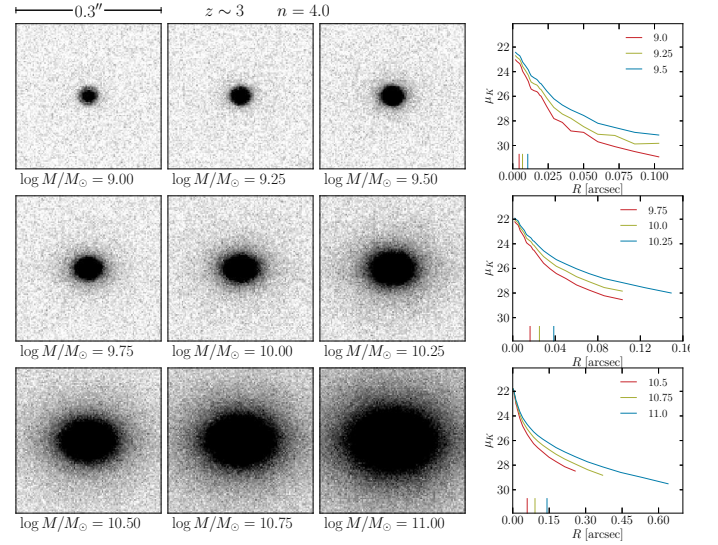
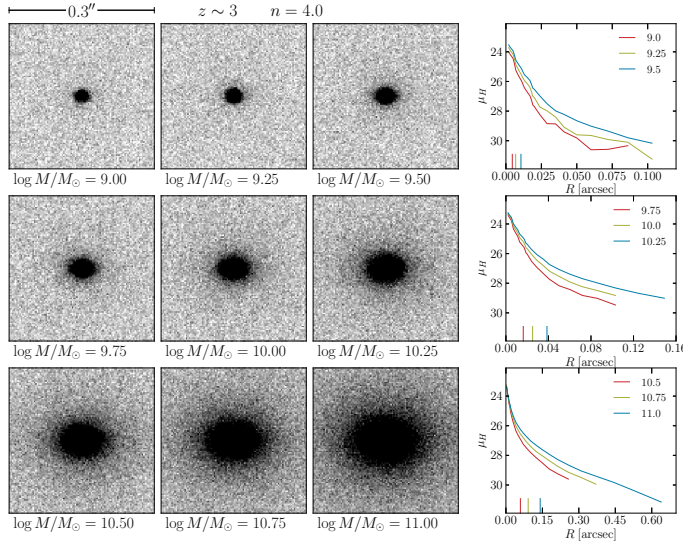


Fig. A.2. As in 2 for H -band images of $z = 3$ galaxies.

Fig. A.3. As in 2 for K -band images of $z = 3$ galaxies.